

Metal Oxide Resistive Memory using Graphene Edge Electrode

Seunghyun Lee^{1*§}, Joon Sohn^{1*}, Zizhen Jiang¹, Hong-Yu Chen^{1,2}, H. -S. Philip Wong¹

¹*Department of Electrical Engineering and Stanford SystemX Alliance, Stanford University, Stanford, California 94305, USA.*

²*Present affiliation: Memory Strategy Group, SanDisk Corporation, 951 SanDisk Drive, Milpitas, CA 95035, USA*

* These authors contributed equally to this work.

§ Corresponding author. Electronic mail: seansl@stanford.edu

The emerging paradigm of “abundant-data” computing requires real-time analytics on enormous quantities of data collected by a mushrooming network of sensors. Today’s computing technology, however, cannot scale to satisfy such big data applications with the required throughput and energy efficiency. The next technology frontier will be monolithically integrated chips with 3-dimensionally interleaved memory and logic for unprecedented data bandwidth with reduced energy consumption. In this work, we exploit the atomically thin nature of the graphene edge to assemble a resistive memory (~3Å thick) stacked in a vertical 3D structure. We report some of the lowest power and energy consumption among the emerging non-volatile memories due to an extremely thin electrode with unique properties, low programming voltages, and low current. Circuit analysis of the 3D architecture using experimentally measured device properties show higher storage potential for graphene devices compared that of metal based devices.

Introduction

The rapid adoption of non-volatile memory technology such as Flash¹ has enabled a revolution in today's mobile computing. To date, the ever-increasing demand for higher density has so far been met through the development of multi-level storage cells and smart peripheral control circuitry that hides the inadequacies and imperfections of the memory cell¹. However, the diminishing amount of stored charges and the increase in bit error rates that accompany feature-size scaling impose significant challenges for the future². Further gains in memory performance and device density will require new breakthroughs in both atomic-scale technology and bit-cost-effective 3D device architectures^{2,3}.

Resistive random access memories (RRAM) based on metal oxide have shown considerable promise as a possible successor to Flash because of better endurance, retention, speed, lower programming voltages, and a higher device density³⁻⁵. These devices also use material sets and fabrication temperatures that are compatible with today's silicon technology^{3,4}, and offer the opportunity for future monolithic three-dimensional integration with logic computation units.

Graphene, an atomically thin crystal lattice of carbon atoms, is known for its unique electronic properties⁶. Both graphene and graphene oxides have been used in various memory devices, including RRAM⁷⁻¹¹, ferroelectric memory¹², and Flash memories¹³ as electrodes and oxides.

In this work, the atomically thin ($\sim 3\text{\AA}$ thick) edge of monolayer graphene was actively used as a SET electrode to form an atomically thin memory structure. We investigate the low energy consumption and the stacking potential of the device in a 3D architecture that is amenable to large scale manufacturing.

Results

Device structure in a 3D vertical cross-point architecture

Two layers of graphene RRAMs (GS-RRAM, GS stands for graphene SET electrode) were stacked to build a 3D vertical cross-point architecture as illustrated in Figs. 1a and b. In the figures, the TiN electrode, the HfO_x layer, and the graphene electrode are depicted in yellow, green, and black, respectively. The fabrication process explained in Supplementary Figure 1 and 2. A transmission electron microscope (TEM) image of the device's cross-section is presented in Figs. 1c-e. The graphene edge contacting the memory element (HfO_x) is highlighted in red. We also fabricated RRAMs based on platinum electrodes (Pt-RRAM) as control devices. The Pt-RRAM (Figs. 1f, g) which was reported previously^{14,15} has the same 3D structure as the GS-RRAM.

Such 3D architectures are part of an ongoing drive in the research community to adopt a bit-cost-effective architecture^{1,2,14-17} with storage densities surpassing that of Flash technology (Supplementary Note 1). From past experimental results¹⁶, the density of a 3D vertical RRAM array is known to be mainly limited by the sheet resistance and the layer thickness of the plane electrode, and not so much by the lithographic half-pitch, as it is in 2D architectures. This is due to the limitation of the pillar electrode resistance and the non-vertical etching angle resulting from trench etching through metal planes¹⁶. Graphene's sheet resistance per thickness (125 Ω per square at a monolayer thickness of 3 Å when doped¹⁸) is significantly lower than that of any metal. All metal films are known to exhibit a steep exponential increase in sheet resistance as the thickness falls below 5 nm¹⁵. Graphene is also significantly easier to etch vertically than metal during pillar formation. Using a well-accepted reliability projection¹⁵—assuming programming voltage of 3V, SiO₂ thickness of 6 nm, half-pitch of 22 nm, and 1° of etch angle improvement—a maximum of

200 stacks will be possible for graphene RRAM as compared to the 60 stacks possible with conventional bulk-metal-based 3D RRAM (Supplementary Table 1).

In both of our RRAM structures, the conductive filaments of oxygen vacancies form at the oxide (HfO_x) similar to conventional metal oxide resistive memories. The number and the size of the conducting filament paths determine the two resistance states of the RRAM: the high resistance state (HRS) and the low resistance state (LRS). In the Pt-RRAM structure (Fig. 1g), TiN is used as the SET electrode as in most conventional devices with TiN-oxide-Pt structures^{4,14}. In the GS-RRAM structure (Figs. 1a-e), however, the graphene electrode is used as the SET electrode to store (SET) and release (RESET) the oxygen ions during the programming process. This is fundamentally different from our previous work¹⁹ on graphene RRAM where the TiN electrode was the SET electrode. The application of graphene as the SET electrode led to power consumption 120 times lower in this work compared to the previous work¹⁹.

The device characteristics of GS-RRAM

A comparison of the typical SET/RESET switching cycle of the GS-RRAM and the Pt-RRAM is shown in Fig. 2a (inset: magnified view of GS-RRAM plot). The SET programming is achieved by applying a positive voltage to the TiN electrode in the Pt-RRAM and a negative voltage to the TiN electrode in the GS-RRAM. The SET/RESET voltage and the RESET current distribution of GS-RRAM and Pt-RRAM after 50 cycles of switching are shown in Figs. 2b and 2c (the values for Pt-RRAM are in agreement with the references^{14,15}). Importantly, the SET/RESET voltages and the RESET currents of GS-RRAM are considerably lower than those of Pt-RRAM. The resistance distributions of both the HRS and the LRS states at 0.1 V bias after 50

cycles for both devices are shown in Fig. 2d. Even with such low programming voltages and current, the memory window is larger for GS-RRAM compared to Pt-RRAM (Fig. 2d).

The power consumption of an RRAM cell is given by the product of the programming voltages and the currents⁴. Due to such low SET/RESET voltages and currents, the power consumption of the GS-RRAM is 300 times lower than that of the Pt-RRAM (Fig. 2e). In fact, the power consumption of the GS-RRAM is one of the lowest compared to recent reports on low power RRAMs (Supplementary Figure 3). From the pulse-mode endurance test with 500 ns width pulse (see Methods), the switching energy (switching voltage \times current \times pulse width = $0.2\text{V} \times 2.3\mu\text{A} \times 500\text{ ns}$) was found to be around 230 fJ. We compared this value with the values of other emerging non-volatile memories, including RRAM, conductive bridge RAM (CBRAM), phase change RAM (PCRAM), and magnetic RAM (MRAM) in Supplementary Figure 4, and found the energy consumption to be comparable to the lowest known values.

The oxygen ion migration and Raman imaging

The mechanism behind the low power/energy consumption can only be explained by first understanding the oxygen ion migration during the switching process. Figures 3b and 3c illustrate the different ways the oxygen ions move and form conductive filaments during the programming process of the Pt-RRAM and the GS-RRAM. For Pt-RRAM, the TiN is the SET electrode and the conducting filaments in the oxide are formed via oxygen migration from HfO_x to the TiN electrode (Fig. 3b)^{4,14}.

In a GS-RRAM, however, a negative voltage is applied to the TiN electrode during the SET process, and the oxygen ions move toward the graphene (Fig. 3c). Unlike in conventional

metal, there will be an electrical potential gradient in graphene since graphene is relatively more resistive ($\sim 6\text{k}\Omega$ per square) than a common metal. Hence, the oxygen ions will not accumulate at the edge but will migrate horizontally in the graphene and the oxide interface. In our previous work²⁰, we have shown how oxygen ions migrate on graphene during the programming process of the RRAM cell by employing Raman spectroscopy (Supplementary Note 2). In this work, the oxygen ion movement was also confirmed by monitoring oxygen dopants in graphene using Raman spectroscopy (Figs. 3d-h, also see Methods). One of the most pronounced indicators of dopants in graphene is the reduction of 2D peak intensity in a Raman spectrum^{20,21}. In Fig. 3d, a typical change in the 2D peak (2670 cm^{-1}) intensity is observed for HRS \rightarrow LRS \rightarrow HRS transition. During the SET process (i.e. HRS \rightarrow LRS), oxygen ions are inserted into the graphene, doping the film. Consequently, a decrease in the 2D peak intensity is observed. During the RESET process, (i.e. LRS \rightarrow HRS) oxygen ions are pushed back into HfO_x from the graphene film. This results in an increase in 2D peak intensity. The Raman peak intensity of silicon (520 cm^{-1}) and the baseline are plotted in parallel to ensure that the references have not changed during measurement (see Methods).

The spatially resolved Raman spectroscopy results for the change in 2D peak intensity during the HRS \rightarrow LRS \rightarrow HRS transition are shown in Figs. 3f, 3g, and 3h, respectively. The blue square in Fig. 3e indicates the Raman-mapped region in the actual device. As the device is switched from HRS to LRS via the SET process, the change in the 2D peak intensity can be readily observed by the contrast difference. The statistical distributions of the changes in 2D peak intensity are also shown as histograms. Noticeable changes in the median values and the standard deviation of the 2D peak intensity are observed as the oxygen ions are inserted into and pushed back from the graphene film. This oxygen migration in graphene is also known to be aided by the Joule heating

generated during the SET/RESET event^{20,22}. Experimental studies also suggest that oxygen can be highly mobile in graphene^{20,22} and can be used as an oxygen capturing layer^{20,23}. As indicated in the literature²⁰, the oxygen may form a covalent bond with the broken bonds of graphene after the SET process, and the process is reversed during the RESET process (Supplementary Figure 5).

The working mechanism

The GS-RRAM offers significantly lower power consumption compared to Pt-RRAM due to three factors: low SET compliance current (Fig. 2a), low RESET current (Fig. 2c), and low programming voltages (Fig. 2b). The Pt-RRAM cannot be operated with such low currents or voltages, and shows severe degradation of the memory window when it is programmed with a lower compliance current (Supplementary Figure 6).

The low SET compliance current in GS-RRAM is possible due to a more resistive HRS and a larger memory window (Fig. 2d) compared to Pt-RRAM. Since the magnitude of the RESET current is directly proportional to the SET compliance current⁴, the low RESET current is also related to these two factors. A systematic breakdown of the resistance components is necessary to understand the differences in LRS/HRS of the two devices (Fig. 4a). Three factors may contribute to the increased resistance of HRS in GS-RRAM compared to Pt-RRAM: the access series resistance R_{series} from the graphene sheet compared to the Pt sheet, the difference of the TiN/oxide ($R_{\text{int,TiN}}$) and graphene/oxide ($R_{\text{int,G}}$) interface, and the different sizes (Figs. 3b and 3c) of filamentary conduction paths in HfO_x ($R_{\text{filament,Pt}}$ and $R_{\text{filament,G}}$). From a transmission line measurement (Supplementary Figure 7 and 8), we found that compared to Pt the additional sheet resistance and the contact resistance of graphene contributed little to the total resistance of HRS. On the other hand, the filamentary resistance and the interfacial resistance between materials (graphene, Pt, or TiN to HfO_x) dominated the total resistance change during the SET/RESET process.

It is known that in an RRAM structure, the resistance of HRS increases as the inverse of the cell area, roughly following Ohm's law⁴. Specifically, the higher HRS of the GS-RRAM compared to Pt-RRAM is closely related to the tail-end thickness of the conducting filaments (CF) in the HRS conditions (Figs. 3b, 3c bottom panels). Because of the thicker Pt electrode edge compared to the graphene edge, the tail end of the CF will be thicker in the Pt-RRAM compared to the ones in the GS-RRAM. This greater thickness results in the more conductive HRS of Pt-RRAM.

The LRS of these devices are related not only to the size of the filaments but also to the different effects of oxygen in the TiN and the graphene electrodes. The LRS of Pt-RRAM (Fig. 2d) is comparable to that of GS-RRAM, even with larger filaments (Figs. 3b, 3c top panel). This is due to the effect of oxygen in TiN. It is fairly well known that oxygen forms a thin $\text{TiO}_x\text{N}_{1-x}$ film in the TiN layer, which works as a barrier against diffusion and carrier transport²⁴. Such a barrier increases the interfacial resistance for Pt-RRAM ($R_{\text{int, TiN}}$), and the total resistance at LRS becomes comparable to that of GS-RRAM.

The low SET/RESET voltage is related to the thickness of the electrode and the oxygen migration mechanism. After the forming process (Supplementary Figure 9), the tip of the conducting filament will be near the top electrode (Fig. 3c). The graphene serving as the SET electrode will have a much stronger electric field at the edge compared to the large TiN electrode because graphene is a monolayer thick. Therefore, a lower SET voltage will be sufficient to pull the oxygen ions from the oxide. On the other hand, we expect the lower RESET voltages are attributed to the lower activation energy for oxygen migration in graphene and the absence of a $\text{TiO}_x\text{N}_{1-x}$ diffusion barrier that is typically formed in TiN electrodes. The activation energy of diffusion for oxygen in graphene (0.15-0.8 eV, carrier density dependent)^{25,26} is known to be lower than that of TiN (0.95-2.1 eV)²⁷. Since the RESET mechanism is closely related to the oxygen

diffusion assisted by Joule heating²⁰ and its activation energy, the required electrical potential for RESET will be lower for the graphene electrode than for the TiN electrode. The temperature-accelerated LRS retention-time measurement can probe the thermal activation of oxygen ion migration from the graphene to the oxide, as shown in Fig. 4b. From the linear fitting of the Arrhenius plot (Methods and Supplementary Figure 10), we estimate the activation energy for oxygen ion migration in graphene to be 0.92 eV, which is lower than the known values for TiN. It is worth noting that the work functions of graphene (4.56 eV) and TiN (4.5 eV) are comparable, and the difference in SET voltages cannot be explained by work function difference alone.

The result of the pulse mode endurance test in Fig. 4c indicated that the GS-RRAM maintained large memory window ($> 70\times$) and showed no sign of deterioration after more than 1600 cycles of switching (Methods). The yield of the GS-RRAM (88%) was also comparable to that of the Pt-RRAM (92%). The reset current and the HRS/LRS characteristics of 10 randomly chosen GS-RRAM devices are shown in Fig. 4d. We also compare the 1st and the 2nd layer devices in Supplementary Figure 11.

3D array simulation

The storage density of a cross-point architecture is ultimately limited by the sneak-path leakage in the half-selected and unselected cells^{16,28,29}. During the write operation, the extra voltage drop along the interconnects caused by the leakage current can lead to an insufficient voltage at the selected cell. During the read operation, parasitic conducting paths in unselected cells can degrade the output signal. To systematically investigate how the sneak-path leakage would limit the bit storage capacity of the 3D memory array, a Simulation Program with an Integrated Circuit Emphasis (HSPICE) circuit simulation^{16,28,29} for the 3D array is performed,

using the experimentally measured device properties (see Methods). Simulations are done using the worst-case data patterns²⁸ with the $0.5 \times V$ write scheme and the column parallel read scheme²⁹. The write margin (V_{access} to the V_{dd} ratio) and the readout margin (ΔI_{read} , the current difference between the on and the off state) as a function of total number of bits for the GS-RRAM and Pt-RRAM arrays are simulated under worst-case conditions assuming 200-layer stacks (Fig. 4e, f). The criteria that limit the total number of array bits during write and read operation are set at 70% and 100nA, respectively. In Figs. 4e and 4f, we observe that the write/read margin for GS-RRAM is larger and its degradation less pronounced, compared to those of Pt-RRAM, as the arrays become larger. This is a direct consequence of smaller pillar resistance enabled by thinner stacks of the graphene plane electrode with lower sheet resistance. Consequently, a larger array of graphene-based RRAM can be assembled without the adverse sneak-path leakage effect.

Discussion

In this work, we demonstrated how the unique advantages of a 2D material can be exploited to outperform conventional materials in today's electronic applications. The E-field from the atomically thin edge electrode and the efficient ion storing/transport mechanism of graphene led to significantly lower power consumption. Graphene was also found to be the key enabler for ultra-high-density, bit-cost-effective 3D RRAM arrays. The increased density and the low power consumption of an RRAM structure will enable significant progress in emerging application areas such as energy-efficient abundant-data computing and neuromorphic computing³⁰. RRAMs employing various oxides have already been demonstrated for spike-timing-dependent plasticity³⁰. A highly integrated electronic synapse network employing low power graphene memory in a bit-

cost-effective 3D architecture will be a significant step toward a highly efficient, next-generation computing system.

Methods

HR TEM sample preparation and imaging

The TEM-ready samples were prepared using the in situ FIB lift-out technique on an FEI Dual Beam FIB/SEM. For the imaging, we used an FEI Tecnai TF-20 FEG/TEM operated at 200kV in bright-field (BF) TEM mode or high-resolution (HR) TEM mode.

Spatially resolved Raman spectroscopy

The images were taken with constant laser intensity right after the SET and the RESET programming. External perturbation was minimized with an oxide capping layer. For the purpose of Raman measurement, single-stack GS-RRAM (without the second stack) was fabricated and measured to eliminate any effect from the second graphene layer. A WiTec 500 AFM/micro-Raman Scanning Microscope was used for the 2D Raman raster scanning of graphene. A 532 nm wavelength was used for all measurements. A $30\mu\text{m} \times 60\mu\text{m}$ area was scanned with an integration time of at least 4 seconds with a $1\mu\text{m}$ resolution. Each measurement was conducted in less than 3 hours.

Extraction of activation energy

The temperature-accelerated LRS retention-time measurement can probe the thermal activation of oxygen ion migration, as shown in Fig. 4b. This will cause the oxygen ions to migrate back to

HfO_x, increasing the resistance (i.e. RESET) of the RRAM. The kinetics of this process can be described by the Arrhenius law.

$$\tau_{reset} = \tau_0 \cdot e^{\frac{E_a}{k_B T}} \quad (1)$$

The τ_{reset} is the characteristic time for RESET transition, τ_0 is a constant, k_B is the Boltzmann constant, E_a is the activation energy barrier, and T is the absolute temperature. The linear fitting result of retention time in logarithmic scale versus reciprocal temperature provides a good estimation of the activation energy (Supplementary Figure 10).

The measurements were done on a semi-automated probe system (Cascade Microtech, Summit) with a temperature controller (Temptronic SA166550). All measurements were done inside the test chamber with the nitrogen gas flowing. The setup was on an anti-vibration table with pneumatic vibration mount. The automated resistance measurement was conducted every 15 seconds to 3 min with 0.1 V bias using a semiconductor parameter analyzer (Agilent 4156C).

Pulse mode endurance test

The pulse mode endurance test was conducted with an Agilent Parameter Analyzer 4155C and an Agilent Pulse generator 81110A connected to a Keithley Switch Matrix 707B. Pulse width was 500 ns with 3s time delay and $\pm 0.2V$ was the read voltage.

HSPICE Simulations on the achievable array size

We adopted the same resistance network and array simulation methodology for the worst-case selected cell of 3D RRAM as in ref^{16,28,29}. The effect of the sneak-path leakage in the achievable array size can be quantified with the write margin ($V_{access} \times V_{dd}^{-1}$) and the readout margin (ΔI_{read}). The definition of V_{access} is the voltage across the accessed cell in the resistance network. ΔI_{read} is defined as the difference in the current flowing through the read resistor (100k Ω) when the RRAM cell is either in the HRS or the LRS. The HRS and the LRS values of GS-RRAM

and Pt-RRAM were extracted from the experimental results of this work. V_{dd} , V_{read} , and $V_{half-bias}$ were set at 5V, 3.5V, and 2V, respectively. The maximum total bits for an array were determined using these criteria. The sheet resistance of Pt¹⁵ and doped graphene¹⁸ was assumed to be 300 Ω per square and 125 Ω per square, respectively. A selector parameter from a published result³¹ was adopted for the simulation. The resistance of the selector was 57.9 M Ω at the half-bias condition and 1k Ω when it was turned on. During read programming, the selector was turned on and the resistance of the LRS of RRAMs was at least 5 times larger than the resistance of the selector during read operation. Feature size was 45 nm with a 12 nm selection material layer inserted in the pillar. The diameter of the Cu metal core was 5 nm and the thickness of TiN was 3 nm. The thickness of HfOx was 5 nm. Hence, the feature size was $2 \times (5+3+12) + 5 = 45$ nm.

References

- 1 Grupp, L. M., Davis, J. D. & Swanson, S. The bleak future of NAND flash memory. *Proceedings of the 10th USENIX conference on File and Storage Technologies*, 2-2 (2012).
- 2 Pirovano, A. & Schuegraf, K. Integrated circuits: Memory grows up. *Nat. Nanotechnol.* **5**, 177-178 (2010).
- 3 Wong, H. S. P. & Salahuddin, S. Memory leads the way to better computing. *Nat. Nanotechnol.* **10**, 191-194 (2015).
- 4 Wong, H.-S. P. *et al.* Metal–oxide RRAM. *Proc. IEEE* **100**, 1951-1970 (2012).
- 5 Waser, R. & Aono, M. Nanoionics-based resistive switching memories. *Nat. Mater.* **6**, 833-840 (2007).
- 6 Novoselov, K. S. *et al.* A roadmap for graphene. *Nature* **490**, 192-200 (2012).
- 7 He, C. *et al.* Nonvolatile resistive switching in graphene oxide thin films. *Appl. Phys. Lett.* **95**, 232101 (2009).
- 8 Yao, J. *et al.* Highly transparent nonvolatile resistive memory devices from silicon oxide and graphene. *Nat. Commun.* **3**, 1101 (2012).
- 9 Jilani, S. M., Gamot, T. D., Banerji, P. & Chakraborty, S. Studies on resistive switching characteristics of aluminum/graphene oxide/semiconductor nonvolatile memory cells. *Carbon* **64**, 187-196 (2013).
- 10 Wang, L.-H. *et al.* The mechanism of the asymmetric SET and RESET speed of graphene oxide based flexible resistive switching memories. *Appl. Phys. Lett.* **100**, 063509 (2012).
- 11 Standley, B. *et al.* Graphene-based atomic-scale switches. *Nano Lett.* **8**, 3345-3349 (2008).

- 12 Zheng, Y. *et al.* Gate-controlled nonvolatile graphene-ferroelectric memory. *Appl. Phys. Lett.* **94**, 163505 (2009).
- 13 Han, S. T. *et al.* Layer-by-Layer-Assembled Reduced Graphene Oxide/Gold Nanoparticle Hybrid Double-Floating-Gate Structure for Low-Voltage Flexible Flash Memory. *Adv. Mater.* **25**, 872-877 (2013).
- 14 Yu, S., Chen, H.-Y., Gao, B., Kang, J. & Wong, H.-S. P. HfO_x-based vertical resistive switching random access memory suitable for bit-cost-effective three-dimensional cross-point architecture. *ACS nano* **7**, 2320-2325 (2013).
- 15 Chen, H.-Y. *et al.* Experimental study of plane electrode thickness scaling for 3D vertical resistive random access memory. *Nanotechnology* **24**, 465201 (2013).
- 16 Yu, S. *et al.* 3D vertical RRAM-Scaling limit analysis and demonstration of 3D array operation. *VLSI Technology (VLSIT), 2013 Symposium on*, T158-T159 (2013).
- 17 Prince, B. *Vertical 3D Memory Technologies*. John Wiley & Sons, Chichester, United Kingdoms, (2014).
- 18 Bae, S. *et al.* Roll-to-roll production of 30-inch graphene films for transparent electrodes. *Nat. Nanotechnol.* **5**, 574-578 (2010).
- 19 Sohn, J., Lee, S., Jiang, Z., Chen, H.-Y. & Wong, H.-S. P. Atomically thin graphene plane electrode for 3D RRAM. in *Electron Devices Meeting, IEEE International*. 5.3.1-5.3.4 (2014).
- 20 Tian, H. *et al.* Monitoring Oxygen Movement by Raman Spectroscopy of Resistive Random Access Memory with a Graphene-Inserted Electrode. *Nano Lett.* **13**, 651-657 (2013).
- 21 Das, A. *et al.* Monitoring dopants by Raman scattering in an electrochemically top-gated graphene transistor. *Nat. Nanotechnol.* **3**, 210-215 (2008).
- 22 Stolyarova, E. *et al.* Observation of graphene bubbles and effective mass transport under graphene films. *Nano Lett.* **9**, 332-337 (2008).
- 23 Ryu, S. *et al.* Atmospheric oxygen binding and hole doping in deformed graphene on a SiO₂ substrate. *Nano Lett.* **10**, 4944-4951 (2010).
- 24 Kwak, J. S. *et al.* Roles of interfacial TiO_xN_{1-x} layer and TiN electrode on bipolar resistive switching in TiN/TiO₂/TiN frameworks. *Appl. Phys. Lett.* **96**, 223502-223503 (2010).
- 25 Suarez, A. M., Radovic, L. R., Bar-Ziv, E. & Sofo, J. O. Gate-voltage control of oxygen diffusion on graphene. *Phys. Rev. Lett.* **106**, 146802 (2011).
- 26 Lee, G., Lee, B., Kim, J. & Cho, K. Ozone adsorption on graphene: ab initio study and experimental validation. *The Journal of Physical Chemistry C* **113**, 14225-14229 (2009).
- 27 Tsetseris, L., Logothetidis, S. & Pantelides, S. Migration of species in a prototype diffusion barrier: Cu, O, and H in TiN. *Appl. Phys. Lett.* **94**, 161903 (2009).
- 28 Liang, J., Yeh, S., Wong, S. S. & Wong, H.-S. Scaling challenges for the cross-point resistive memory array to sub-10nm node-an interconnect perspective. in *Memory Workshop, 4th IEEE International*. 1-4 (2012).
- 29 Chen, H.-Y. *et al.* HfO_x based vertical resistive random access memory for cost-effective 3D cross-point architecture without cell selector. in *Electron Devices Meeting (IEDM), 2012 IEEE International*. 20.27. 21-20.27. 24 (IEEE).
- 30 Yu, S. *et al.* A Low Energy Oxide-Based Electronic Synaptic Device for Neuromorphic Visual Systems with Tolerance to Device Variation. *Adv. Mater.* **25**, 1774-1779 (2013).

- 31 Govoreanu, B. *et al.* Thin-Silicon Injector (TSI): an All-Silicon Engineered Barrier, Highly Nonlinear Selector for High Density Resistive RAM Applications. in *Memory Workshop, IEEE International*. 69 (2015).

Additional information Supplementary information is available in the online version of the paper. Reprints and permissions information is available online at www.nature.com/reprints. Correspondence and requests for materials should be addressed to S.L. (seansl@stanford.edu).

Acknowledgements This work is supported in part by the Office of the Director of National Intelligence (ODNI), Intelligence Advanced Research Projects Activity (IARPA) Trusted Integrated Circuits (TIC) Program (Program Directors: Dennis Polla and Carl McCants), and the member companies of Stanford Non-Volatile Memory Technology Research Initiative (NMTRI) affiliate program, and Systems on Nanoscale Information Fabrics (SONIC) Center, one of six centers of Semiconductor Technology Advanced Research Network (STARnet), a Semiconductor Research Corporation (SRC) program sponsored by Microelectronics Advanced Research Corporation (MARCO) and Defense Advanced Research Projects Agency (DARPA). J. Sohn is additionally supported by the STX foundation scholarship for overseas studies. Hong-Yu Chen is additionally supported by the Intel Ph.D. Fellowship.

Part of the work was conducted in the Stanford Nanofabrication Facility (SNF) at Stanford University, a member of the National Nanotechnology Infrastructure Network funded by the National Science Foundation.

Author contributions S.L., J.S. and H.S.P.W. conceived the experiments. S.L. and J.S. fabricated the devices, developed the electrical measurement set-up and performed the measurements. H.Y.C. provided support for fabrication. Z.J. performed the simulations based on experimental device

properties. S.L., J.S. wrote the paper and H.S.P.W. supervised the work. All authors discussed the results and commented on the manuscript.

Competing financial interests The authors declare no competing financial interests

Figure Captions

Figure 1 Structure of graphene based and Pt based RRAM in a vertical 3D cross-point architecture. **a**, An illustration of graphene-based RRAM in a vertical cross-point architecture. The RRAM cells are formed at the intersections of the TiN pillar electrode and the graphene plane electrode. The resistive switching HfOx layer surrounds the TiN pillar electrode and is also in contact with the graphene plane electrode. **b**, A schematic cross-section of the graphene-based RRAM. **c**, HR-TEM image (details in Methods) of the two-stack graphene RRAM structure. The RRAM memory elements are highlighted in red. The scale bar is 40nm. **d,e**, First and second layer of GS-RRAM with graphene on top of the Al₂O₃ layer. The scale bars are 5 nm. **(f), (g)**, TEM image of the two-stack Pt based RRAM from previous work^{14,15}. The scale bar is 40 nm for **(f)** and 5 nm for **(g)**.

Figure 2 The device characteristics of GS-RRAM compared to Pt-RRAM and other emerging memory devices. **a**, Typical DC I-V switching characteristics of GS-RRAM and Pt-RRAM. For Pt-RRAM, SET process is observed when positive voltage is applied to TiN. For GS-RRAM, SET process is observed when positive voltage is applied to graphene. The SET compliances for G-mode, T-mode, and Pt-RRAM are 5 μ A, 10 μ A, and 80 μ A, respectively for optimum conditions. A magnified plot of GS-RRAM is shown as inset. **b**, The SET and RESET voltage distribution of GS-RRAM and Pt-RRAM after 50 cycles of switching. The SET/RESET

voltages of GS-RRAM are noticeably lower (inset). **c**, Reset current distribution of GS-RRAM and Pt-RRAM after 50 cycles. GS-RRAM exhibit much lower reset current compared to Pt-RRAM. **d**, Resistance distribution after 50 cycles for GS-RRAM and Pt-RRAM at 0.1V. Larger memory windows are observed for GS-RRAM compared to Pt-RRAM. **e**, Reset power distribution of GS-RRAM and Pt-RRAM. The power consumption of GS-RRAM is 300 times lower than that of Pt-RRAM. This is from the combined effect of lower programming voltages and currents.

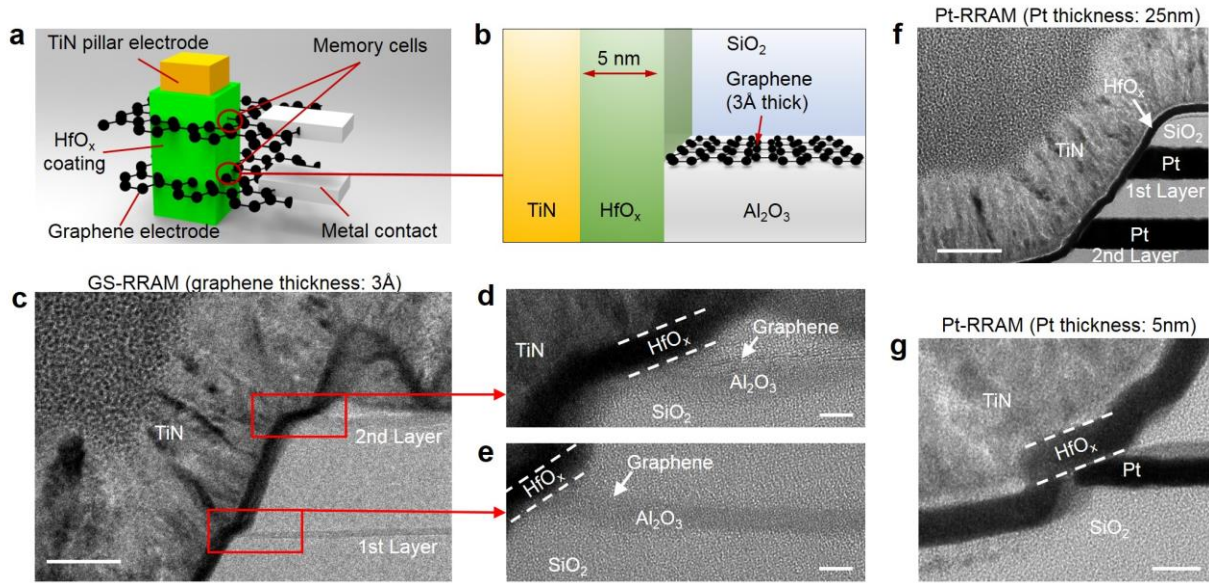
Figure 3 The working mechanism and spatially resolved Raman imaging of oxygen ions in graphene during subsequent SET/RESET process of GS-RRAM

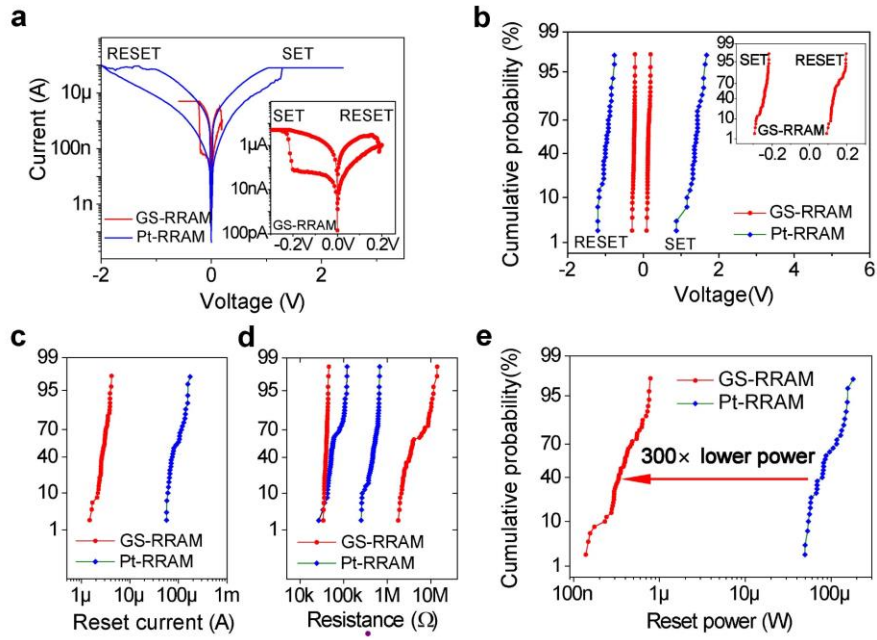
a, Illustrations of the GS-RRAM structure. **b**, Working mechanism of Pt-RRAM. SET process (oxygen vacancy filament formation) is achieved by applying positive voltage to the TiN electrode. **c**, Working mechanism of GS-RRAM. The SET process is achieved by applying positive voltage to graphene instead of the TiN electrode. Notice the opposite direction of oxygen ion movement in GS-RRAM compared to Pt-RRAM. **d**, Changes in the 2D peak intensity as the oxygen is inserted (SET) and extracted (RESET) from the graphene film. The laser intensity was kept constant during the measurements. Notice that the reference silicon peak (520 cm^{-1}) is not changing during this transition. **e**, A microscopic image of the Raman mapped area highlighted in blue. The scale bar is $15\text{ }\mu\text{m}$. **f,g,h**, 2-dimensional Raman scanning of the 2D peak intensity in the mapped area before programming (f), after oxygen ions are inserted into graphene via SET process (g), and after oxygen ions are pulled out from graphene via RESET process (h). All three images have the same color scale for 2D peak intensity and the laser intensity was kept constant during the measurements (See Methods). The darker hue is observed for graphene with the oxygen ions in (g). The scale bar is $10\text{ }\mu\text{m}$. The statistical distributions of the 2D peak intensity changes are also

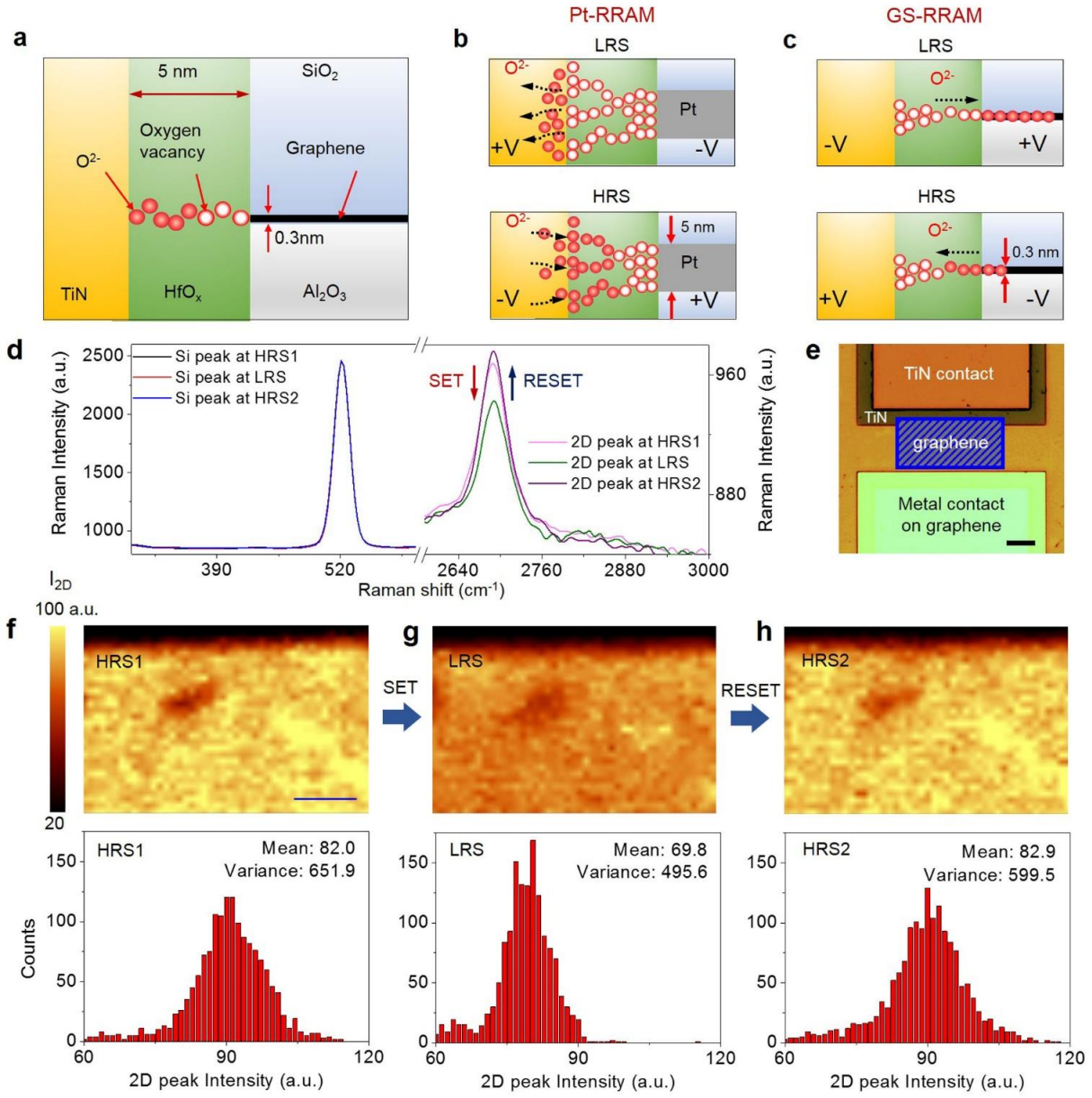
shown as histograms. Noticeable changes in the median values are observed as the oxygen ions are inserted into and pulled out from the graphene film.

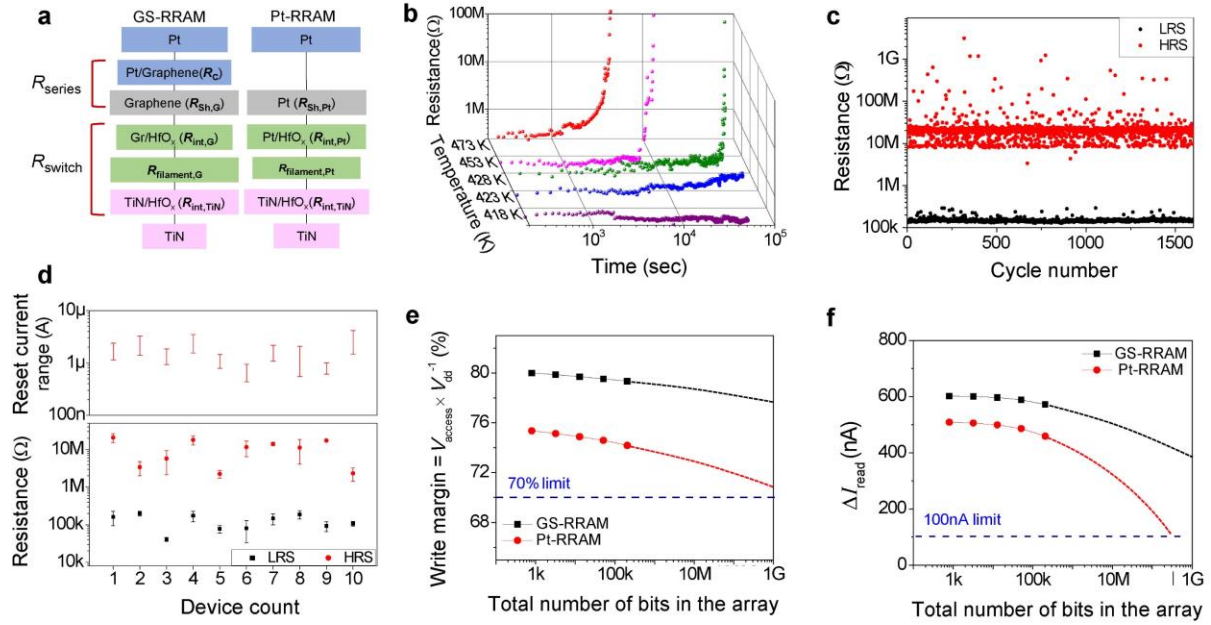
Figure 4 Resistance component breakdown, retention, pulse endurance, device variations, and array performance of stacked GS-RRAM.

a, Resistance component breakdown of GS-RRAM and Pt-RRAM. In comparison to Pt-RRAM, GS-RRAM has 4 different resistance components: Pt/graphene contact resistance (R_C), graphene film resistance ($R_{sh,G}$), graphene/HfO_x interface resistance ($R_{int,G}$), and the thickness of the conduction filaments ($R_{Filament,G}$). **b**, Temporal evolution of GS-RRAM LRS resistance at temperatures ranging from 418K to 473K near 0.1V bias. Elevated temperatures were used in this study to obtain the critical time (i.e. filament rupture time) for oxygen migration within a reasonable time frame (See Methods). **c**, Pulse endurance test of GS-RRAM. Device switched with over 70× difference in HRS and LRS, and suffered no read/write disturbance after more than 1600 cycles. **d**, The maximum to minimum reset current distribution (top) and HRS/LRS resistance distribution after 50 cycles (bottom) for 10 randomly chosen GS-RRAMs. The cycle-to-cycle variations are shown as error bars which represent one standard deviation for each case. All devices were measured under the SET compliance current of 5 μA. The worst case scenario still exhibits HRS to LRS ratio exceeding 10×. **e**, Write margin comparison of Pt-RRAM and GS-RRAM for a 3D architecture with 200 stacks. **f**, Read margin comparison between Pt-RRAM and GS-RRAM for a 3D architecture with 200 stacks.

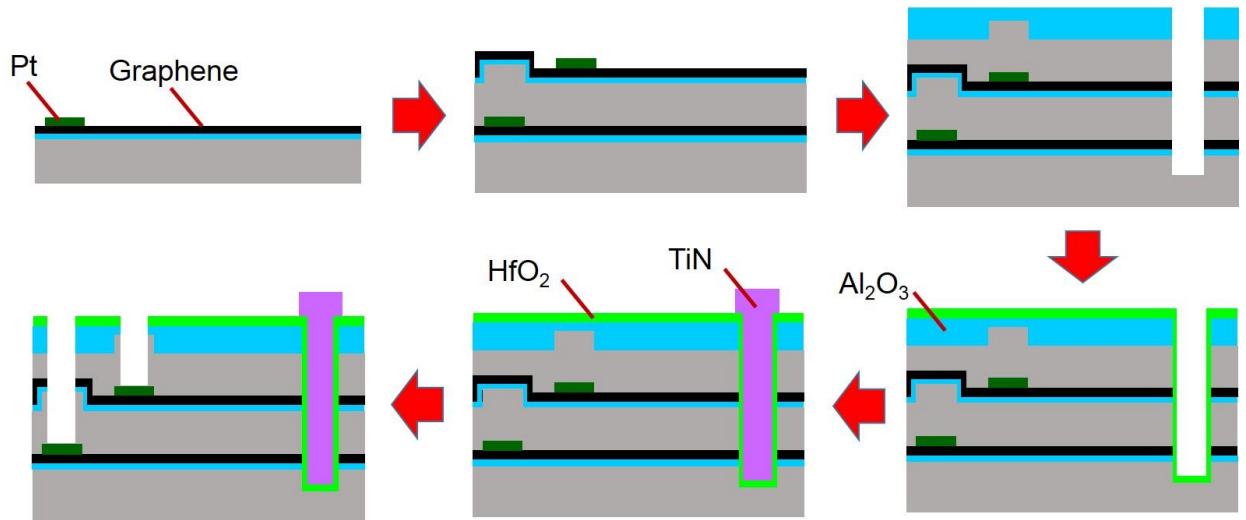




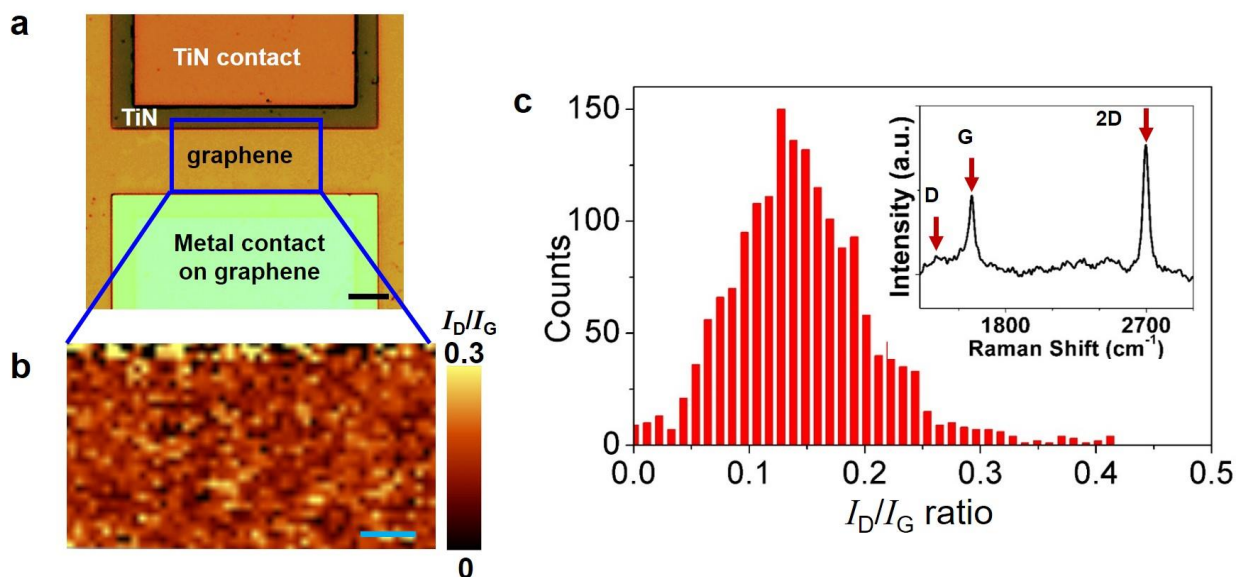




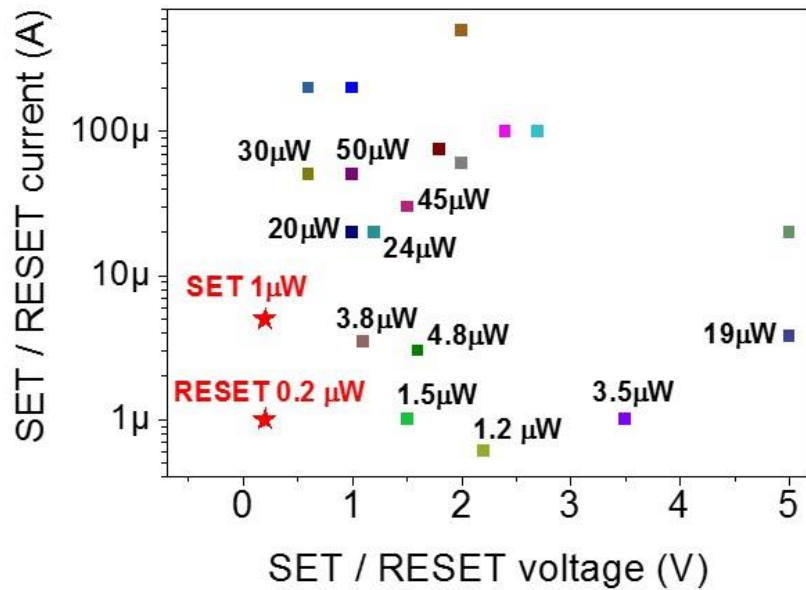
Supplementary Figures



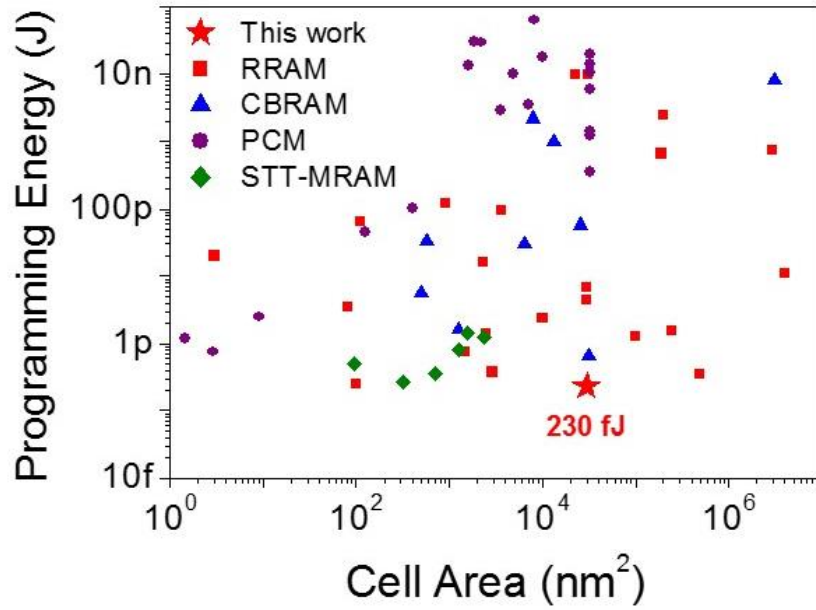
Supplementary Figure 1 Fabrication process. The devices were fabricated via sequential transfer of graphene, metal contact deposition, deep trench etching, HfO_2 deposition (atomic layer deposition) followed by TiN pillar formation (sputtering and lift-off). A thin layer (5nm) of Al_2O_3 was deposited before the graphene transfer process to promote graphene adhesion to the surface. First, single layer graphene is transferred on to a dielectric surface with 5 nm Al_2O_3 and 100 nm of SiO_2 . The transfer method is identical to the previous works¹⁻³. Monolayer graphene grown on copper foil with chemical vapour deposition method was purchased (Single Layer Graphene on Copper foil: 2 inch \times 2inch, Graphene supermarket) and the monolayer quality was confirmed with Raman spectroscopy (Supplementary Figure 2c). Ti/Pt (3 nm/30 nm) layers are deposited by evaporation and patterned by lift-off process. 60 nm of SiO_2 (LPCVD) is deposited. Then these processes are repeated twice for two layers of single layer graphene; 50 nm ALD Al_2O_3 is deposited on the top layer for etch hard mask. A trench is etched down to the bottom SiO_2 layer followed by 5nm of HfO_x (ALD) which is conformally deposited as the active resistive switching layer and 200 nm of TiN electrode is deposited by sputtering and patterned via lift-off. The contacts are opened via dry etching.



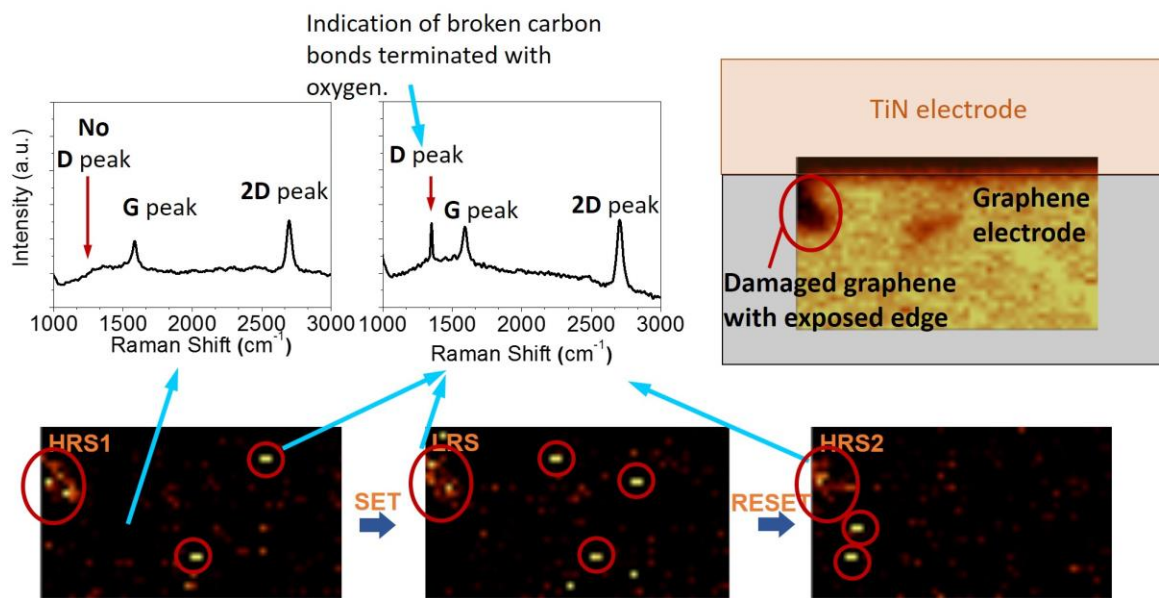
Supplementary Figure 2 Verification of graphene thickness and quality. **a**, Actual device image. The Raman laser scanned area is highlighted in blue. The scale bar is $15\ \mu\text{m}$. **b**, A 2D Raman spectra map of D peak to G peak ratio (I_D/I_G) after the complete fabrication process. This ratio is a known indicator of the disorders in graphene films. The I_D/I_G value is limited to approximately 0.1, indicating a low defect density in the film⁴. The inset shows a typical Raman spectrum of monolayer graphene with weak D-peak intensity after the complete fabrication process. Minimized physical disturbance and the low fabrication temperature ($<300\ \text{°C}$) were essential to maintaining the high quality graphene. The scale bar is $10\ \mu\text{m}$. **c**, A histogram of I_D/I_G ratio of Supplementary Figure 2b. The median value is 0.12. A typical Raman spectrum of the scanned area is shown as the inset.



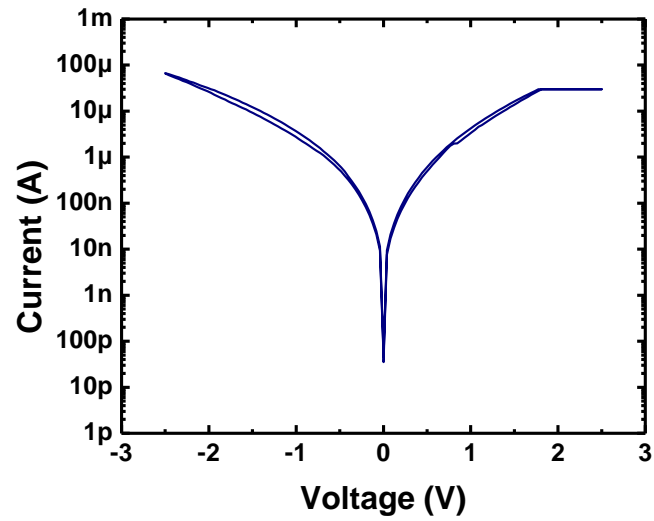
Supplementary Figure 3 Comparison of power consumption. Programming voltages, currents, and power consumptions from the recent reports⁵⁻²³ on low power RRAMs were plotted. With one of the lowest SET/RESET voltages ever recorded, the SET and the RESET power consumption of the demonstrated GS-RRAM (shown as red stars above) exhibit extremely low values. From a practical application point of view, the process that consumes the most power (SET or RESET) is plotted for other works, since the larger value determines the power delivery requirements for the chip.



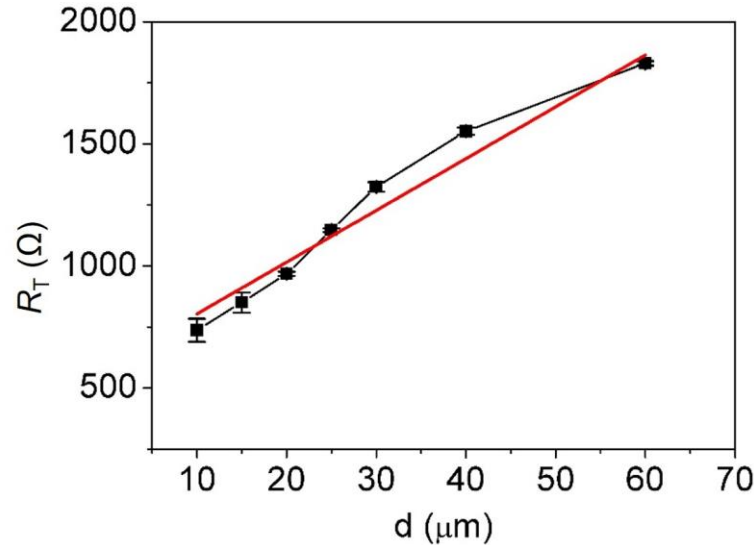
Supplementary Figure 4 Comparison of energy consumption. Comparison of programming energy for GS-RRAM and other emerging non-volatile memories with respect to cell area. The switching energy for GS-RRAM is one of the lowest. RRAM references are ^{5,11,24-47}, CBRAM references are ⁴⁸⁻⁵⁶, PCM references are ⁵⁷⁻⁷⁶, and STT-MRAM references are ^{77,78}, respectively.



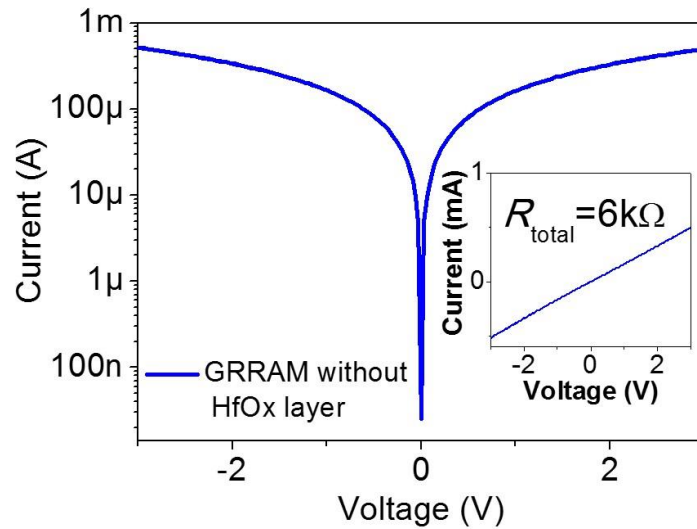
Supplementary Figure 5 Oxygen bonding in the graphene electrode. Although graphene is widely known to be inert, the edge and the broken bonds at the defect sites are more active compared to the basal plane of the graphene sheet. Typical graphene oxide Raman signature is the pronounced D peak⁷⁹. (The intensity of G peak, on the other hand, is associated with the number of graphene layers and this may or may not be related to the graphene oxide.) D peak is also a strong indication of broken carbon bonds (i.e. dislocations, defects) and is pronounced in graphene ribbons with the edges exposed. These broken carbon bonds are more likely to be terminated with oxygen atoms. We specifically found an area in one of devices where the graphene was damaged and the edge was exposed. This edge is composed of broken carbon bonds similar to defects/dislocations at the basal plane and can be detected with the D peak intensity map as shown below in Supplementary Figure 3. An interesting aspect is that the defect region (bright area) highlighted with red circles seems to be created/annihilated (or even shifted) after consecutive SET and RESET process. Several past research results confirm that graphene broken bonds (dislocations) can be created/annihilated and shifted depending on which state is more thermodynamically favorable^{80,81}. More importantly, this indicate that these oxygen binding phenomenon is reversible as previous work⁸² suggested. As indicated in the reference⁸², the oxygen may form a covalent bond at the defect sites of graphene after the SET process and the process is reversed during the RESET process. Another important observation is that the point defects seems to be created and annihilated randomly but at the edge, the bright colored region is pervasive regardless of whether it is after the SET or the RESET process. This may indicate that the edge is always oxidized when it is in contact with the HfO_x . The oxidized edge seems to have little effect on switching endurance of the device. We have switched the device more than 1600 times to observe that the memory function did not degrade (Fig. 4c).



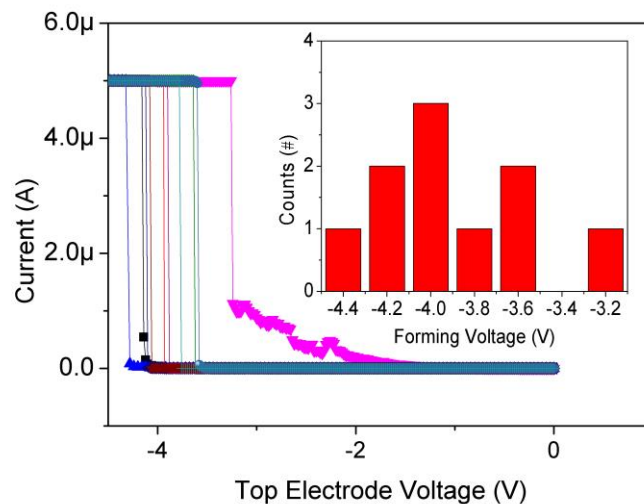
Supplementary Figure 6 Degradation of memory window for Pt-RRAM with 30 μA SET compliance. Pt-RRAM devices with lower SET compliance than 80 μA suffers from memory window degradation as shown in the plot. This is expected since PtRRAM's HRS is significantly more conductive compared to GRRAM due to the larger area of the Pt bottom (passive) electrode.



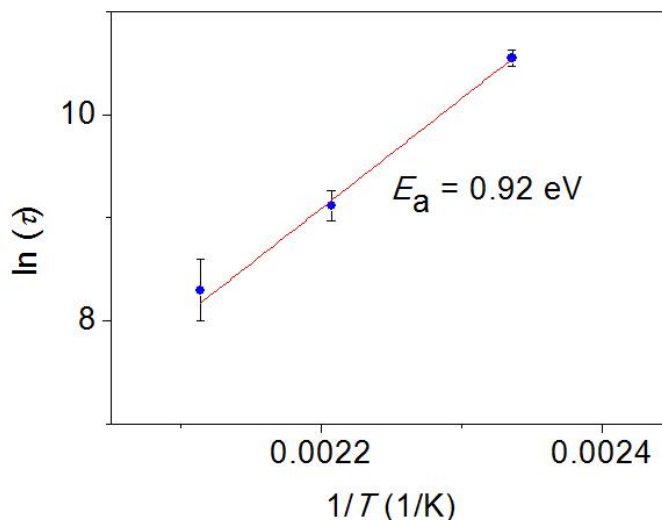
Supplementary Figure 7 Total resistance value from the as-fabricated wafer with circular transmission line test structure⁸³ as a function of gap distance. From the Y-intercept = $2R_C = 591\Omega$. The corresponding contact resistance R_C between the graphene and the metal (Ti/Pt) contact was found to be 295Ω with specific contact resistance of $9.3\Omega\cdot\text{cm}$. With the slope of $21.2\ \Omega\ \mu\text{m}^{-1}$, the sheet resistance of graphene ($R_{\text{sh,G}}$) is extracted to be $6.7\text{k}\Omega$ per square. Pristine, exfoliated graphene without environmental doping is reported to have sheet resistance value of $\sim 6\ \text{k}\Omega$ per square.⁸⁴ From our I_D/I_G Raman map (Supplementary Figure 2), the defect level was not significant after dielectric deposition (LTO, 300°C). Considering the low D-peak level in our graphene, the resulting $R_{\text{sh,G}}$ is in close agreement with that of a pristine graphene that is void of any dopants or defects⁸⁵⁻⁸⁷. Since the measurements are done on the as-fabricated wafers, small discrepancies may arise from the process conditions. For Ti/Pt layer (Ti 1 nm/Pt 5 nm), the sheet resistance $R_{\text{sh,Pt}}$ was extracted to be 558Ω from 20 TLM measurements. The Pt sheet resistance is also in agreement with the literature⁸⁸. Graphene is approximately $\times 20$ thinner than the Ti/Pt layer and $\times 12$ more resistive, showing slightly superior conductance with similar thicknesses. However, it should be noted that atomically thin metal such as Pt layer tends to form discontinuous island, and a sharp nonlinear increase in sheet resistance is observed as the thickness decreases⁸⁸.



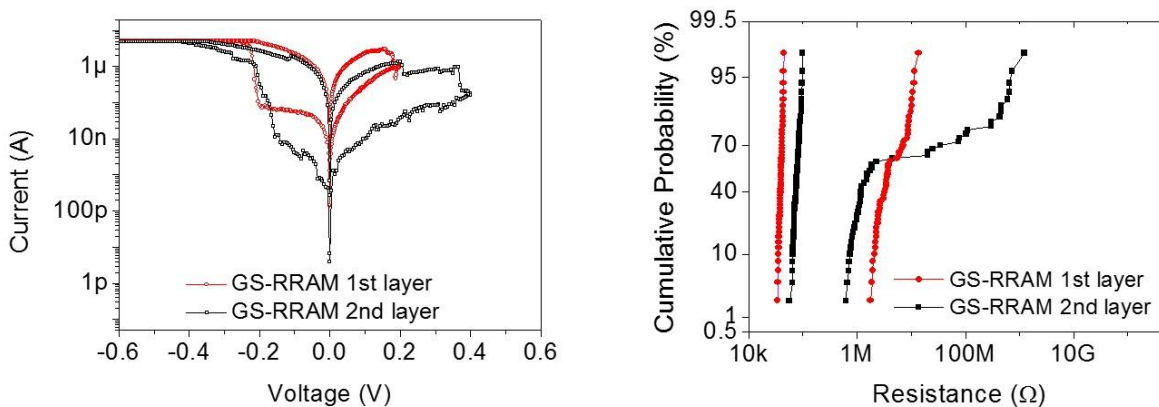
Supplementary Figure 8 The I-V curve of GS-RRAM without the HfOx layer (inset: linear scale). The I-V curve of GS-RRAM without the HfOx layer (inset: linear scale). The total resistance of the GS-RRAM device *without* the HfO₂ is close to 6 kΩ, which is only a fraction of HRS resistance. This strongly indicates that the series resistance R_{series} (i.e. $R_{\text{sh,G}} + R_{\text{c}}$) of GS-RRAM is not the major factor that contributes to the increases of the HRS resistance in GS-RRAM. On the contrary, this outcome suggests that the difference between the R_{switch} of GS-RRAM ($R_{\text{int,G}} + R_{\text{filament,G}}$) and Pt-RRAM ($R_{\text{int,Pt}} + R_{\text{filament,Pt}}$) determines the HRS of GS-RRAM and Pt-RRAM, respectively.



Supplementary Figure 9 Forming of GS-RRAM. The top electrode is the TiN electrode during the forming process. Forming curves are collected from 10 cells with 5 μA compliance current. Inset: forming voltage distribution.



Supplementary Figure 10 Arrhenius type plot of the wait time versus $1/T$ extracted from Fig. 4b. The sudden transitions to the OFF state in Fig. 4b corresponds to the rupture of the oxygen vacancy based filament by the diffusion of oxygen ion towards HfO_x layer. The activation energy of the barriers can be extracted from temperature dependence of the characteristic dwell time for RESET transition (Arrhenius equation in Methods). From the linear fitting of retention time in logarithm scale versus reciprocal temperature, we estimate of the activation energy E_a for ion migration in graphene to be 0.92 eV.



Supplementary Figure 11 Typical DC I-V switching and HRS/LRS characteristics of bottom layer and top layer of GS-RRAM. The GS-RRAM in the bottom layer exhibited even lower RESET current with similar SET voltages. However, there were some discrepancies in the RESET voltages for bottom and top layer. Importantly, the overall RESET power is still similar due to lower RESET current. Qualitatively similar memory windows were observed for top and bottom devices. The lowest memory window in the second layer is still above $10\times$.

Supplementary Table

| | Thickness in nm (Electrode+SiO ₂) | <i>F</i> = 20 nm | <i>F</i> = 22 nm | <i>F</i> = 26 nm |
|---------------------------------|--|------------------|------------------|------------------|
| Etch ratio 30 Etch Angle 88° | 11nm (Pt=5nm) | 54 | 60 | 70 |
| | 16nm (Pt=10nm) | 37 | 41 | 48 |
| | 21nm (Pt=15nm) | 28 | 31 | 37 |
| Etch Angle 89° | 6.3nm (graphene=0.3nm) | 181 | 200 | 236 |

Supplementary Table 1 Analysis of the number of achievable stacks with a dielectric thickness of 6nm. The achievable number of stacks can be calculated using the equation for reliability projection from reference ⁸⁸. Total stack height = $R \times F / T$ (R is the etching aspect ratio, F is the lithographic half pitch, and T is the combined thickness of the plane electrode and the dielectric in between). Assuming SiO₂ thickness of 6 nm, half-pitch of 22nm, and etch angle increase of just 1°, the maximum graphene RRAM stacks possible will be 200 stacks compared to the 60 stacks possible with Pt-RRAM. With an operating voltage of 0.2V in our GS-RRAM and a higher etching angle, we expect the number of possible graphene RRAM stacks to increase even more since a thinner dielectric can be used.

Supplementary Notes

Supplementary Note 1 3D vertical cross-point architectures

A pressing imperative for RRAM technology is to adopt a bit-cost-effective 3D architecture satisfying the requirements of performance metrics (density, latency, and energy consumption), which surpass those of 3D stackable multi-bit NAND Flash technology. Many industry/research groups⁸⁹⁻⁹³ are actively working on variations of 3D vertical cross-point architectures as shown in Supplementary Fig. S1. The graphene RRAM in this work (with pillar electrode and planar graphene electrode) is compatible with all the 3D vertical cross-point architectures recently introduced⁸⁹⁻⁹³.

The integration density of such 3D architectures depends on the number of stacks which is limited by the plane electrode thickness, the sheet resistance of the plane electrode, the dielectric thickness (related to the programming voltages and cross-talk), the pillar etch angle, the lithographic pitch, and the resistance of the pillar/plane electrode^{88,94}.

Since the total pillar height is limited, a thin device structure will be important for ultra-high density storage^{88,94}. However, there is a fundamental limitation on how thin the metal plane electrode can be.

There has been a recent report of an RRAM structure with a sub-5nm thick vertical TiN electrode⁹⁵. Although it is possible to form such sub-5nm metal electrodes, the main challenge lies not in the thickness of the metal, but in the high sheet resistance. All metal films are known to exhibit a steep exponential increase in sheet resistance as the thickness decreases under 10 nm^{88,96}. This is because extremely thin metal films tend to form discontinuous islands, and thin dielectric layers are formed on the grain boundaries⁹⁶. Such high sheet resistance of the plane electrode will result in a significant voltage drop on the electrode and severely degrade the write/read margin of the 3D RRAM structure^{88,94}, which limits the integration density. Hence, producing a sub-5nm conducting film with a low enough sheet resistance for 3D RRAM is a difficult task without using special methods or materials.

Graphene's sheet resistance per thickness is significantly lower than that of any metal. Graphene has been experimentally proven through the use of doping technique⁹⁷ to have sheet resistance as low as 125 - 200 Ω per square^{1,86,97} with a monolayer thickness. These levels of resistance are something impossible to achieve (at such thickness) with conventional metal. From the measurements, graphene exhibited superior sheet resistance value per thickness (i.e. graphene is 20 \times thinner and 12 \times more resistive) compared to Pt after fabrication (Supplementary Section 7). Considering the nonlinear increase of Pt sheet resistance in such a scale, the actual sheet resistance of Pt when it is as thin as graphene will be drastically higher.

It is also important to note that metal contact to graphene is an ohmic contact, and the contact resistance is relatively low due to the graphene's semi-metallic nature⁹⁷. An optimized

metal/graphene specific contact resistivity is $7.5 \times 10^{-8} \Omega \text{ cm}^2$ ⁹⁸. This value is smaller than that of both Al and Pt contact to degenerately N-doped silicon ($2 \times 10^{20} \text{ cm}^{-3}$) as shown in⁹⁹.

From the analysis in the previous work⁸⁸, the required dielectric thickness is approximately 6 nm of SiO₂ in between each layer if the devices are to work with operating voltages of 3V (much higher than the 0.2V required for our GS-RRAM). The 6 nm SiO₂ is required since it can maintain a lifetime > 10 years at the operating voltage of 3V based on the breakdown voltage and the time dependent dielectric breakdown (TDDB) lifetime extrapolation for PECVD SiO₂ sandwiched between metal electrodes¹⁰⁰. Finally, graphene (3Å) is significantly easier to etch vertically than Pt (6nm) during pillar formation. (Graphene is simply etched with weak O₂ plasma treatment.) This property is highly beneficial since the etch angle is a very important factor that determines the number of achievable stacks^{88,94}.

Supplementary Note 2 Comparison of using graphene as an oxygen detector (previous work, ref⁸²) and for oxygen storage (this work)

In RRAM devices, the resistive switching is attributed to the formation (SET) and the subsequent rupture (RESET) of nanoscale conductive filaments involving oxygen ion migration^{14,101-106}. A generally accepted theory claims that the filament formation is based on the oxygen ion movement from the switching material.

It is fairly well known that the oxygen function as dopants in graphene, and the doping level of graphene can be observed with Raman spectroscopy^{82,107,108}. We have previously monitored the oxygen ion in a RRAM structure by inserting graphene film between the TiN layer and HfO_x⁸².

The memory structures in our previous work and the current work are very different. In the previous work, the SET electrode is the TiN and the RESET electrode is the Pt. In our work, the SET electrode is the graphene edge and the RESET electrode is the TiN. Also the previous work is a planar structure and the current work is a vertical structure.

Although both previous and current work report low power consumption, the mechanisms for achieving low power consumption are fundamentally different. In the previous work, the low power was due to reduced RESET current from the high built-in series resistance of inter-layer graphene. The overall SET/RESET voltages (~2V) have few differences between structures “with” and “without” graphene interlayer.

In the current work, we see a drastic difference in SET/RESET voltages between GS-RRAM (~0.2V) and the Pt-based device (~1.5 to 2V). This is because the graphene, instead of the TiN layer, is used as the SET electrode. Here we are using graphene as a stand-alone oxygen reservoir, unlike in the previous work. The lowering of SET/RESET voltage is related to the lack of a TiO_xN_{1-x} barrier layer in the HfO_x/graphene interface, and the ease of oxygen diffusion across the graphene electrode as explained in the main text.

Supplementary References

- 1 Lee, S., Lee, K., Liu, C.-H. & Zhong, Z. Homogeneous bilayer graphene film based flexible transparent conductor. *Nanoscale* **4**, 639-644 (2012).
- 2 Lee, S., Lee, K. & Zhong, Z. Wafer scale homogeneous bilayer graphene films by chemical vapor deposition. *Nano Lett.* **10**, 4702-4707 (2010).
- 3 Lee, S., Lee, K., Liu, C.-H., Kulkarni, G. S. & Zhong, Z. Flexible and transparent all-graphene circuits for quaternary digital modulations. *Nat. Commun.* **3**, 1018 (2012).
- 4 Lucchese, M. M. *et al.* Quantifying ion-induced defects and Raman relaxation length in graphene. *Carbon* **48**, 1592-1597 (2010).
- 5 Lee, H. *et al.* Low power and high speed bipolar switching with a thin reactive Ti buffer layer in robust HfO₂ based RRAM. in *Electron Devices Meeting, IEEE International*. 1-4 (2008).
- 6 Lee, H.-Y. *et al.* Low-power switching of nonvolatile resistive memory using hafnium oxide. *Jpn. J. Appl. Phys.* **46**, 2175 (2007).
- 7 Cheng, C. H., Yeh, F. S. & Chin, A. Low-Power High-Performance Non-Volatile Memory on a Flexible Substrate with Excellent Endurance. *Adv. Mater.* **23**, 902-905 (2011).
- 8 Wu, M.-C., Lin, Y.-W., Jang, W.-Y., Lin, C.-H. & Tseng, T.-Y. Low-power and highly reliable multilevel operation in 1T1R RRAM. *IEEE Electron Device Lett.* **32**, 1026-1028 (2011).
- 9 Wu, Y., Lee, B. & Wong, H.-S. Ultra-low power Al₂O₃-based RRAM with 1μA reset current. in *VLSI Technology Systems and Applications, International Symposium on*. 136-137 (2010).
- 10 Goux, L., Lisoni, J. G., Wang, X. P., Jurczak, M. & Wouters, D. J. Optimized Ni oxidation in 80-nm contact holes for integration of forming-free and low-power Ni/NiO/Ni memory cells. *Electron Devices, IEEE Transactions on* **56**, 2363-2368 (2009).
- 11 Tsunoda, K. *et al.* Low power and high speed switching of Ti-doped NiO ReRAM under the unipolar voltage source of less than 3 V. in *Electron Devices Meeting, IEEE International*. 767-770 (2007).
- 12 Hou, T.-H. *et al.* Evolution of RESET current and filament morphology in low-power HfO₂ unipolar resistive switching memory. *Appl. Phys. Lett.* **98**, 103511 (2011).
- 13 Lee, H. *et al.* Low-power and nanosecond switching in robust hafnium oxide resistive memory with a thin Ti cap. *IEEE Electron Device Lett.* **31**, 44-46 (2010).
- 14 Wong, H.-S. P. *et al.* Metal-oxide RRAM. *Proc. IEEE* **100**, 1951-1970 (2012).
- 15 Wang, J.-C. *et al.* Low-power and high-reliability gadolinium oxide resistive switching memory with remote ammonia plasma treatment. *Jpn. J. Appl. Phys.* **52**, 04CD07 (2013).
- 16 Bai, Y. *et al.* Low power W: AlO_x/WO_x bilayer resistive switching structure based on conductive filament formation and rupture mechanism. *Appl. Phys. Lett.* **102**, 173503 (2013).
- 17 Yang, L. *et al.* Linear scaling of reset current down to 22-nm node for a novel RRAM. *IEEE Electron Device Lett.* **33**, 89-91 (2012).
- 18 Shima, H. *et al.* Voltage polarity dependent low-power and high-speed resistance switching in CoO resistance random access memory with Ta electrode. *Appl. Phys. Lett.* **93**, 113504 (2008).
- 19 Cheng, C. *et al.* Highly uniform low-power resistive memory using nitrogen-doped tantalum pentoxide. *Solid-State Electron.* **73**, 60-63 (2012).

- 20 Raghavan, N. *et al.* Very low reset current for an RRAM device achieved in the oxygen-vacancy-controlled regime. *IEEE Electron Device Lett.* **32**, 716-718 (2011).
- 21 Walczyk, C. *et al.* Pulse-induced low-power resistive switching in HfO₂ metal-insulator-metal diodes for nonvolatile memory applications. *Journal of Applied Physics* **105**, 114103-114103-114106 (2009).
- 22 Cheng, C., Chin, A. & Yeh, F. Novel ultra-low power RRAM with good endurance and retention. in *VLSI Technology, Symposium on.* 85-86 (2010).
- 23 Wu, Y., Yu, S., Lee, B. & Wong, P. Low-power TiN/Al₂O₃/Pt resistive switching device with sub-20 μ A switching current and gradual resistance modulation. *J. Appl. Phys.* **110**, 094104 (2011).
- 24 Baek, I. *et al.* Highly scalable nonvolatile resistive memory using simple binary oxide driven by asymmetric unipolar voltage pulses. in *Electron Devices Meeting, IEEE International.* 587-590 (2004).
- 25 Chen, A. *et al.* Non-volatile resistive switching for advanced memory applications. in *Electron Devices Meeting, IEEE International.* 746-749 (2005).
- 26 Wei, Z. *et al.* Highly reliable TaO_x ReRAM and direct evidence of redox reaction mechanism. in *Electron Devices Meeting, IEEE International.* 1-4 (2008).
- 27 Tseng, Y. H., Huang, C.-E., Kuo, C., Chih, Y.-D. & Lin, C. J. High density and ultra small cell size of contact ReRAM (CR-RAM) in 90nm CMOS logic technology and circuits. in *Electron Devices Meeting (IEDM), 2009 IEEE International.* 1-4 (2009).
- 28 Wang, X. *et al.* Highly compact 1T-1R architecture (4F² footprint) involving fully CMOS compatible vertical GAA nano-pillar transistors and oxide-based RRAM cells exhibiting excellent NVM properties and ultra-low power operation. in *Electron Devices Meeting (IEDM), 2012 IEEE International.* 20.26. 21-20.26. 24 (2012).
- 29 Shen, W. C. *et al.* High-K metal gate contact RRAM (CRRAM) in pure 28nm CMOS logic process. in *Electron Devices Meeting (IEDM), 2012 IEEE International.* 31.36. 31-31.36. 34 (2012).
- 30 Kim, S. *et al.* Ultrathin (<10nm) Nb₂O₅/NbO₂ hybrid memory with both memory and selector characteristics for high density 3D vertically stackable RRAM applications. in *VLSI Technology (VLSIT), 2012 Symposium on.* 155-156 (2012).
- 31 Chen, H.-Y. *et al.* HfO_x based vertical resistive random access memory for cost-effective 3D cross-point architecture without cell selector. in *Electron Devices Meeting (IEDM), 2012 IEEE International.* 20.27. 21-20.27. 24 (2012).
- 32 Wu, Y. *et al.* First Demonstration of RRAM Patterned by Block Copolymer Self-Assembly. in *Electron Devices Meeting (IEDM), 2013 IEEE International.* 1-20.28 (2013).
- 33 Li, K.-S. *et al.* Utilizing Sub-5 nm sidewall electrode technology for atomic-scale resistive memory fabrication. in *VLSI Technology (VLSI-Technology): Digest of Technical Papers, 2014 Symposium on.* 1-2 (2014).
- 34 Sohn, J., Lee, S., Jiang, Z., Chen, H.-Y. & Wong, H.-S. P. Atomically thin graphene plane electrode for 3D RRAM. in *Electron Devices Meeting (IEDM), 2014 IEEE International.* 5.3. 1-5.3. 4 (2014).
- 35 Sekar, D. *et al.* Technology and circuit optimization of resistive RAM for low-power, reproducible operation. in *Electron Devices Meeting (IEDM), 2014 IEEE International.* 28.23. 21-28.23. 24 (2014).

- 36 Jo, S. H., Kumar, T., Narayanan, S., Lu, W. D. & Nazarian, H. 3D-stackable crossbar resistive memory based on field assisted superlinear threshold (FAST) selector. in *Electron Devices Meeting (IEDM), 2014 IEEE International*. 6.7. 1-6.7. 4 (2014).
- 37 Lee, B. & Wong, H.-S. NiO resistance change memory with a novel structure for 3D integration and improved confinement of conduction path. in *VLSI Technology, 2009 Symposium on*. 28-29 (2009).
- 38 Chen, Y. *et al.* Highly scalable hafnium oxide memory with improvements of resistive distribution and read disturb immunity. in *Electron Devices Meeting (IEDM), 2009 IEEE International*. 1-4 (2009).
- 39 Sakotsubo, Y. *et al.* A new approach for improving operating margin of unipolar ReRAM using local minimum of reset voltage. in *VLSI Technology (VLSIT), 2010 Symposium on*. 87-88 (2010).
- 40 Ho, C. *et al.* 9nm half-pitch functional resistive memory cell with $<1\mu\text{A}$ programming current using thermally oxidized sub-stoichiometric WO_x film. in *Electron Devices Meeting (IEDM), 2010 IEEE International*. 19.11. 11-19.11. 14 (2010).
- 41 Chien, W. *et al.* A forming-free WO_x resistive memory using a novel self-aligned field enhancement feature with excellent reliability and scalability. in *Electron Devices Meeting (IEDM), 2010 IEEE International*. 19.12. 11-19.12. 14 (2010).
- 42 Cheng, C., Tsai, C., Chin, A. & Yeh, F. High performance ultra-low energy RRAM with good retention and endurance. in *Electron Devices Meeting (IEDM), 2010 IEEE International*. 19.14. 11-19.14. 14 (2010).
- 43 Lee, J. *et al.* Diode-less nano-scale $\text{ZrO}_x/\text{HfO}_x$ RRAM device with excellent switching uniformity and reliability for high-density cross-point memory applications. in *Electron Devices Meeting (IEDM), 2010 IEEE International*. 19.15. 11-19.15. 14 (2010).
- 44 Tran, X. *et al.* High performance unipolar $\text{AlO}_y/\text{HfO}_x/\text{Ni}$ based RRAM compatible with Si diodes for 3D application. in *VLSI Technology (VLSIT), 2011 Symposium on*. 44-45 (2011).
- 45 Yi, J. *et al.* Highly reliable and fast nonvolatile hybrid switching ReRAM memory using thin Al_2O_3 demonstrated at 54nm memory array. in *VLSI Technology (VLSIT), 2011 Symposium on*. 48-49 (2011).
- 46 Kim, Y.-B. *et al.* Bi-layered RRAM with unlimited endurance and extremely uniform switching. in *VLSI Technology (VLSIT), 2011 Symposium on*. 52-53 (2011).
- 47 Govoreanu, B. *et al.* $10\times 10\text{nm}^2$ Hf/HfO_x crossbar resistive RAM with excellent performance, reliability and low-energy operation. in *Electron Devices Meeting (IEDM), 2011 IEEE International*. 31.36. 31-31.36. 34 (2011).
- 48 Aratani, K. *et al.* A novel resistance memory with high scalability and nanosecond switching. in *Electron Devices Meeting, 2007. IEDM 2007. IEEE International*. 783-786 (2007).
- 49 Sakamoto, T. *et al.* A Ta_2O_5 solid-electrolyte switch with improved reliability. in *VLSI Technology, 2007 IEEE Symposium on*. 38-39 (2007).
- 50 Lin, Y.-Y. *et al.* A novel TiTe buffered Cu-GeSbTe/ SiO_2 electrochemical resistive memory (ReRAM). in *VLSI Technology (VLSIT), 2010 Symposium on*. 91-92 (2010).
- 51 Wang, M. *et al.* A novel $\text{Cu}_x\text{Si}_y\text{O}$ resistive memory in logic technology with excellent data retention and resistance distribution for embedded applications. in *VLSI Technology (VLSIT), 2010 Symposium on*. 89-90 (2010).

- 52 Vianello, E. *et al.* Sb-doped GeS₂ as performance and reliability booster in Conductive Bridge RAM. in *Electron Devices Meeting (IEDM), 2012 IEEE International*. 31.35. 31-31.35. 34 (2012).
- 53 Goux, L. *et al.* Field-driven ultrafast sub-ns programming in W\Al₂O₃Ti\CuTe-based 1T1R CBRAM system. in *VLSI Technology (VLSIT), 2012 Symposium on*. 69-70 (2012).
- 54 Guy, J. *et al.* Investigation of the physical mechanisms governing data-retention in down to 10nm Nano-trench Al₂O₃/CuTeGe Conductive Bridge RAM (CBRAM). in *Proc. IEEE IEDM*. (2013).
- 55 Vianello, E. *et al.* Resistive memories for ultra-low-power embedded computing design. in *Electron Devices Meeting (IEDM), 2014 IEEE International*. 6.3. 1-6.3. 4 (2014).
- 56 Sills, S. *et al.* A copper ReRAM cell for Storage Class Memory applications. in *VLSI Technology (VLSI-Technology): Digest of Technical Papers, 2014 Symposium on*. 1-2 (2014).
- 57 Yi, J. *et al.* Novel cell structure of PRAM with thin metal layer inserted GeSbTe. in *Electron Devices Meeting, 2003. IEDM'03 Technical Digest. IEEE International*. 37.33. 31-37.33. 34 (2003).
- 58 Pirovano, A. *et al.* Scaling analysis of phase-change memory technology. in *Electron Devices Meeting, 2003. IEDM'03 Technical Digest. IEEE International*. 29.26. 21-29.26. 24 (2003).
- 59 Matsui, Y. *et al.* Ta₂O₅ interfacial layer between GST and W plug enabling low power operation of phase change memories. in *Electron Devices Meeting, 2006. IEDM'06. International*. 1-4 (2006).
- 60 Mantegazza, D., Ielmini, D., Varesi, E., Pirovano, A. & Lacaíta, A. Statistical analysis and modeling of programming and retention in PCM arrays. in *Electron Devices Meeting, 2007. IEDM 2007. IEEE International*. 311-314 (2007).
- 61 Chen, W. *et al.* A novel cross-spacer phase change memory with ultra-small lithography independent contact area. in *Electron Devices Meeting, 2007. IEDM 2007. IEEE International*. 319-322 (2007).
- 62 Annunziata, R. *et al.* Phase change memory technology for embedded non volatile memory applications for 90nm and beyond. in *Electron Devices Meeting (IEDM), 2009 IEEE International*. 1-4 (2009).
- 63 Fantini, A. *et al.* N-doped GeTe as performance booster for embedded phase-change memories. in *Electron Devices Meeting (IEDM), 2010 IEEE International*. 29.21. 21-29.21. 24 (2010).
- 64 Lee, S. *et al.* Highly productive PCRAM technology platform and full chip operation: Based on 4F² (84nm pitch) cell scheme for 1 Gb and beyond. in *Electron Devices Meeting (IEDM), 2011 IEEE International*. 3.3. 1-3.3. 4 (2011).
- 65 Cheng, H. *et al.* A high performance phase change memory with fast switching speed and high temperature retention by engineering the Ge_xSb_yTe_z phase change material. in *Electron Devices Meeting (IEDM), 2011 IEEE International*. 3.4. 1-3.4. 4 (2011).
- 66 Morikawa, T. *et al.* A low power phase change memory using low thermal conductive doped-Ge₂Sb₂Te₅ with nano-crystalline structure. in *Electron Devices Meeting (IEDM), 2012 IEEE International*. 31.34. 31-31.34. 34 (2012).
- 67 Cheng, H. *et al.* Atomic-level engineering of phase change material for novel fast-switching and high-endurance PCM for storage class memory application. *IEDM Tech. Dig*, 758-761 (2013).

- 68 Ha, Y. *et al.* An edge contact type cell for phase change RAM featuring very low power consumption. in *VLSI Technology, 2003. Digest of Technical Papers. 2003 Symposium on.* 175-176 (2003).
- 69 Pellizzer, F. *et al.* Novel μ trench phase-change memory cell for embedded and stand-alone non-volatile memory applications. in *VLSI Technology, 2004. Digest of Technical Papers. 2004 Symposium on.* 18-19 (2004).
- 70 Breitwisch, M. *et al.* Novel lithography-independent pore phase change memory. in *VLSI Technology, 2007 IEEE Symposium on.* 100-101 (2007).
- 71 Kim, I. *et al.* High performance PRAM cell scalable to sub-20nm technology with below $4F^2$ cell size, extendable to DRAM applications. in *VLSI Technology (VLSIT), 2010 Symposium on.* 203-204 (2010).
- 72 Liang, J., Jeyasingh, R. G. D., Chen, H.-Y. & Wong, H.-S. A $1.4\mu\text{A}$ reset current phase change memory cell with integrated carbon nanotube electrodes for cross-point memory application. in *VLSI Technology (VLSIT), 2011 Symposium on.* 100-101 (2011).
- 73 Bedeschi, F. *et al.* An 8Mb demonstrator for high-density 1.8 V phase-change memories. in *VLSI Circuits, 2004. Digest of Technical Papers. 2004 Symposium on.* 442-445 (2004).
- 74 Oh, H. Enhanced write performance of a 64Mb phase-change random access memory. in *IEEE International Solid State Circuits Conference.* **1**, 48-584 (2005).
- 75 Kang, S. *et al.* A $0.1\mu\text{m}$ 1.8V 256Mb 66Mhz synchronous burst pram. in *2006 IEEE International Solid State Circuits Conference-Digest of Technical Papers.* 487-496 (2006).
- 76 Hanzawa, S. *et al.* A 512kB embedded phase change memory with 416kB/s write throughput at $100\mu\text{A}$ cell write current. in *Solid-State Circuits Conference, 2007. ISSCC 2007. Digest of Technical Papers. IEEE International.* 474-616 (2007).
- 77 Gajek, M. *et al.* Spin torque switching of 20 nm magnetic tunnel junctions with perpendicular anisotropy. *Appl. Phys. Lett.* **100**, 132408 (2012).
- 78 Sato, H. *et al.* Properties of magnetic tunnel junctions with a MgO/CoFeB/Ta/CoFeB/MgO recording structure down to junction diameter of 11 nm. *Appl. Phys. Lett.* **105**, 062403 (2014).
- 79 Wu, N. *et al.* Synthesis of network reduced graphene oxide in polystyrene matrix by a two-step reduction method for superior conductivity of the composite. *J. Mater. Chem.* **22**, 17254-17261 (2012).
- 80 Lehtinen, O., Kurasch, S., Krasheninnikov, A. & Kaiser, U. Atomic scale study of the life cycle of a dislocation in graphene from birth to annihilation. *Nat. Commun.* **4** (2013).
- 81 Kurasch, S. *et al.* Atom-by-atom observation of grain boundary migration in graphene. *Nano Lett.* **12**, 3168-3173 (2012).
- 82 Tian, H. *et al.* Monitoring Oxygen Movement by Raman Spectroscopy of Resistive Random Access Memory with a Graphene-Inserted Electrode. *Nano Lett.* **13**, 651-657 (2013).
- 83 Klootwijk, J. & Timmering, C. Merits and limitations of circular TLM structures for contact resistance determination for novel III-V HBTs. in *2004 international conference on microelectronic test structures.* 247-252 (2004).
- 84 Wang, Q. H., Kalantar-Zadeh, K., Kis, A., Coleman, J. N. & Strano, M. S. Electronics and optoelectronics of two-dimensional transition metal dichalcogenides. *Nat. Nanotechnol.* **7**, 699-712 (2012).
- 85 Bonaccorso, F., Sun, Z., Hasan, T. & Ferrari, A. Graphene photonics and optoelectronics. *Nat. Photonics* **4**, 611-622 (2010).

- 86 Wang, Y., Tong, S. W., Xu, X. F., Özyılmaz, B. & Loh, K. P. Interface Engineering of Layer - by - Layer Stacked Graphene Anodes for High - Performance Organic Solar Cells. *Adv. Mater.* **23**, 1514-1518 (2011).
- 87 Blake, P. *et al.* Graphene-based liquid crystal device. *Nano Lett.* **8**, 1704-1708 (2008).
- 88 Chen, H.-Y. *et al.* Experimental study of plane electrode thickness scaling for 3D vertical resistive random access memory. *Nanotechnology* **24**, 465201 (2013).
- 89 Yu, S., Chen, H.-Y., Gao, B., Kang, J. & Wong, H.-S. P. HfO_x-based vertical resistive switching random access memory suitable for bit-cost-effective three-dimensional cross-point architecture. *ACS nano* **7**, 2320-2325 (2013).
- 90 Cha, E. *et al.* Nanoscale (~10nm) 3D vertical RRAM and NbO₂ threshold selector with TiN electrode. in *Electron Devices Meeting (IEDM), 2013 IEEE International*. 10.15. 11-10.15. 14 (2013).
- 91 Deng, Y. *et al.* Design and Optimization Methodology for 3D RRAM Arrays. in *IEEE International Electron Devices Meeting (IEDM)*. 9-11 (2013).
- 92 Hsu, C.-W. *et al.* 3D Vertical TaO_x/TiO₂ RRAM with over 10³ Self-Rectifying Ratio and Sub- μ A Operating Current. *IEEE Int. Electron Devices Meet. Tech. Dig*, 10-13 (2013).
- 93 Cha, E. *et al.* Nanoscale (10nm) 3d vertical reram and Nbo₂ threshold selector with tin electrode. in *Proceedings of the IEEE International Electron Devices Meeting (IEDM)*. 10.15 (2013).
- 94 Yu, S. *et al.* 3D vertical RRAM-Scaling limit analysis and demonstration of 3D array operation. *VLSI Technology (VLSIT), 2013 Symposium on*, T158-T159 (2013).
- 95 Li, K.-S. *et al.* Utilizing sub-5 nm sidewall electrode technology for atomic-scale resistive memory fabrication. in *Symp. VLSI Technology*. p131-132 2014.
- 96 Zhigal'skii, G. P. & Jones, B. K. *The Physical Properties of Thin Metal Films*. (Taylor & Francis, 2003).
- 97 Bae, S. *et al.* Roll-to-roll production of 30-inch graphene films for transparent electrodes. *Nat. Nanotechnol.* **5**, 574-578 (2010).
- 98 Robinson, J. A. *et al.* Contacting graphene. *Appl. Phys. Lett.* **98**, 053103 (2011).
- 99 Yu, A. Electron tunneling and contact resistance of metal-silicon contact barriers. *Solid-State Electron.* **13**, 239-247 (1970).
- 100 Zhang, G., Hu, C., Yu, P., Chiang, S. & Hamdy, E. Metal-to-metal antifuses with very thin silicon dioxide films. *IEEE Electron Device Lett.* **15**, 310-312 (1994).
- 101 Guan, X., Yu, S. & Wong, H.-S. On the switching parameter variation of metal-oxide RRAM—Part I: Physical modeling and simulation methodology. *Electron Devices, IEEE Transactions on* **59**, 1172-1182 (2012).
- 102 Yu, S., Guan, X. & Wong, H.-S. On the switching parameter variation of metal oxide RRAM—Part II: Model corroboration and device design strategy. *Electron Devices, IEEE Transactions on* **59**, 1183-1188 (2012).
- 103 Yang, Y. *et al.* Observation of conducting filament growth in nanoscale resistive memories. *Nat. Commun.* **3**, 732 (2012).
- 104 Kwon, D.-H. *et al.* Atomic structure of conducting nanofilaments in TiO₂ resistive switching memory. *Nat. Nanotechnol.* **5**, 148-153 (2010).
- 105 Lee, M.-J. *et al.* Electrical manipulation of nanofilaments in transition-metal oxides for resistance-based memory. *Nano Lett.* **9**, 1476-1481 (2009).
- 106 Waser, R. & Aono, M. Nanoionics-based resistive switching memories. *Nat. Mater.* **6**, 833-840 (2007).

- 107 Das, A. *et al.* Monitoring dopants by Raman scattering in an electrochemically top-gated graphene transistor. *Nat. Nanotechnol.* **3**, 210-215 (2008).
- 108 Tongay, S. *et al.* Rectification at graphene-semiconductor interfaces: zero-gap semiconductor-based diodes. *Physical Review X* **2**, 011002 (2012).